agricultural engineering.eu 80(1), 2025, 35–52

DOI:10.15150/ae.2025.3329

agricultural
engineering.eu

Field contour and obstacle detection for automated agricultural machinery: A multi-temporal segmentation method based on Sentinel-2 satellite data

Steffen Metzger, Marcus Geimer

The increasing automation of agricultural machinery allows operators of these machines to carry out additional activities during harvesting, among other things, which can reduce the subjective mental workload in cognitively undemanding situations. As these activities distract the operator from the driving task, it is important to know the environmental conditions precisely. This includes the field contour and points of interest (POI), such as obstacles. In order for operators to perform additional tasks in a potentially obstructed field, these important areas that require increased attention must be identified. This article presents a method to identify the contour of the field and the POIs. For this purpose, freely available Sentinel-2 satellite data is used. The image data is processed with a multitemporal region growing segmentation. A total of ten different fields in northern Germany were examined. The selection of seed points and the parameter values were empirically analyzed and optimized. This method leads to satisfactory results if suitable satellite image data and seed points are used. The mean Jaccard Index (JI) across all selected fields is 0.913.

Keywords
Automation and robotics in agriculture, assistance systems, satellite data, image segmentation

Problem statement and introduction

The demographic shift and the increasing demands for balancing work and family life have led to a growing number of individuals abandoning agriculture or deciding not to pursue this profession in the first place (Pascher et al. 2020). The “Fahrerkabine 4.0” research project aims to promote the development of young talent in agriculture by designing an attractive working environment on the combine harvester. The optimized working environment should help agricultural employees to perform their tasks satisfactorily, effectively and efficiently.

Due to the complex work processes of a combine harvester and the increasing automation of the machines, the operator of such a machine experiences many inhomogeneous external workload conditions. However, De Waard (1996) showed that the ideal mental workload state of an operator is in the medium mental workload range. Monotony (very low mental workload) and mental overload should be avoided, as this reduces performance and well-being. A fundamental goal of the “Fahrerkabine 4.0” project is to reduce the operator’s mental workload peaks and thus increase well-being (Metzger et al. 2022b). Advances in automation make it possible to suggest targeted task recommendations to the operator in the form of possible activities during phases of reduced mental workload.

received 19 January 2024 | accepted 5 December 2024 | published 27 January 2025

The activities can range from machine-related setting checks and watching training videos to private communication and the use of social media. In addition, tasks that would normally have to be completed after field work, such as documentation duties and private and professional organizational activities, can be carried out (Metzger et al. 2022a). This can significantly improve the work-life balance, as overtime can be reduced during the harvest period. It is also possible to provide assistance in phases of higher mental workload.

To enable the operator to shift focus away from the driving task and to propose targeted recommendations or actions to the user, various boundary conditions must be known (Metzger et al. 2022a). On the one hand, the user's current state of mental workload must be known, which is detected by eye-tracking parameters and pulse measurement and passed on to the system. Secondly, the system must have knowledge of the environment to be able to suggest task recommendations in situations where the user is susceptible. The field contour is particularly important for the environmental conditions, as the turning process of the combine harvester, for example, can be a challenging task for the operator, even with automated turning. This is mainly due to the fact that objects and other obstacles can accumulate at the edges of the field due to surrounding structures such as woodland and traffic routes. However, there are also irregularities and structures in the field that require the operator's increased attention. Storage crops, electricity pylons and wind turbines are particularly worth mentioning in this context.

Other agricultural machines, such as tractors, are also suitable for the use of such an assistance system and the method for field contour and obstacle detection. Although the work processes in a combine harvester are demanding due to the specific focus on harvesting, they are less varied within the harvesting period than the numerous possible applications of a tractor, which are given by the various attachments. However, since not all situations and functions of a combine harvester can yet be fully automated, an operator is absolutely essential for these important moments. However, the operator mainly takes on an observing role, which makes him more susceptible to distracting activities in the form of task recommendations. In the following, the field contour and obstacle detection is first examined using the example of a combine harvester.

In view of the fact that a sufficient and production-ready environment sensor system for large-scale obstacle detection is expensive and has so far only been implemented in specific autonomous machine types in series machines, an alternative approach is presented below (CLAAS Gruppe 2023, Caes 2022). One promising method is remote sensing with satellite data.

Material and methods

Initial satellite data

There are currently a large number of earth observation satellites that could be used for remote sensing with the aim of field contour and obstacle detection. Table 1 shows the different missions and their specific resolutions. They were selected based on their level of popularity and their ability to provide high-resolution data on land masses. (Airbus Defence and Space 2019, DigitalGlobe 2014, Fletcher 2012, Planet Labs 2016, U.S. Geological Survey 2019)

Table 1: Overview of selected earth observation missions with the respective resolution of the satellites

Mission	Spatial resolution in m	Spectral resolution in channels	Time resolution in days
Sentinel-2	10 20 60	13	5
Landsat 8	15 30	11	16
Spot 7	1.5 6	5	1–3
World View 3	0.31 1.24 3.7 30	29	< 1
Rapideye	6.5	5	< 5.5

In principle, a higher resolution, both in terms of time, space and spectral resolution, is more advantageous for the following results than a lower resolution. However, as the missions with very high resolution are only commercially available, the Sentinel-2 satellites of the ESA's Copernicus program are used in this case. Although Landsat 8 is also free of charge, it offers a lower spatial and temporal resolution in comparable channels. The Sentinel satellites offer a suitable spatial and temporal resolution on the one hand and 13 different spectral channels from 443 nm to 2190 nm on the other. These channels can be used to form special indices to obtain further information. The most widely used index for the detection of vegetation is the Near Difference Vegetation Index (NDVI) (Bhandari et al. 2012). There are numerous vegetation indices, many of which are based on the Normalized Difference Vegetation Index (NDVI). An example of this is the Enhanced Vegetation Index (EVI), which specializes in the evaluation of canopy (Huete et al. 2002), whereas the NDVI generally considers the chlorophyll of the vegetation. The NDVI is therefore considered representative in the following. In an empirical comparison, the Normalized Difference Water Index (NDWI) also delivered very good results, which is why it is also considered below. The NDWI is mainly used to detect water surfaces, but can also be used very well to detect vegetation (McFeeters 1996). The NDVI is calculated as follows:

$$NDVI = \frac{NIR-RED}{NIR+RED} \quad \text{(Eq. 1)}$$

NIR denotes the wavelength of the near infrared range and therefore band 8 in the case of the Sentinel-2 spectrum. RED stands for the wavelength range of visible red light and therefore band 4 of the Sentinel-2 spectrum. As the reflectance of the NIR spectrum increases significantly in healthy vegetation compared to visible light, vegetation can be recognized very well with this index (Kuechly et al. 2020). The NDWI is calculated slightly modified as follows:

$$NDWI = \frac{GREEN-NIR}{GREEN+NIR} \quad \text{(Eq. 2)}$$

Both NDWI and NDVI image data can be used in the following steps.

Process steps

An overview of the overall algorithm is shown in Figure 1. The algorithm can be broken down into three different process steps. The pre-process includes the initial data acquisition with dynamically adapted requirement profiles for the data providers of the respective satellite data. The two sub-processes of the main process take place in the subsequent process step. On the one hand, the field contour detection algorithm is executed, and on the other, the obstacle detection based on it, which is carried out exclusively in the already detected field for optimization reasons. Finally, the collected results from the previous steps are prioritized and merged in the post-process to obtain a combined field contour and obstacle mask.

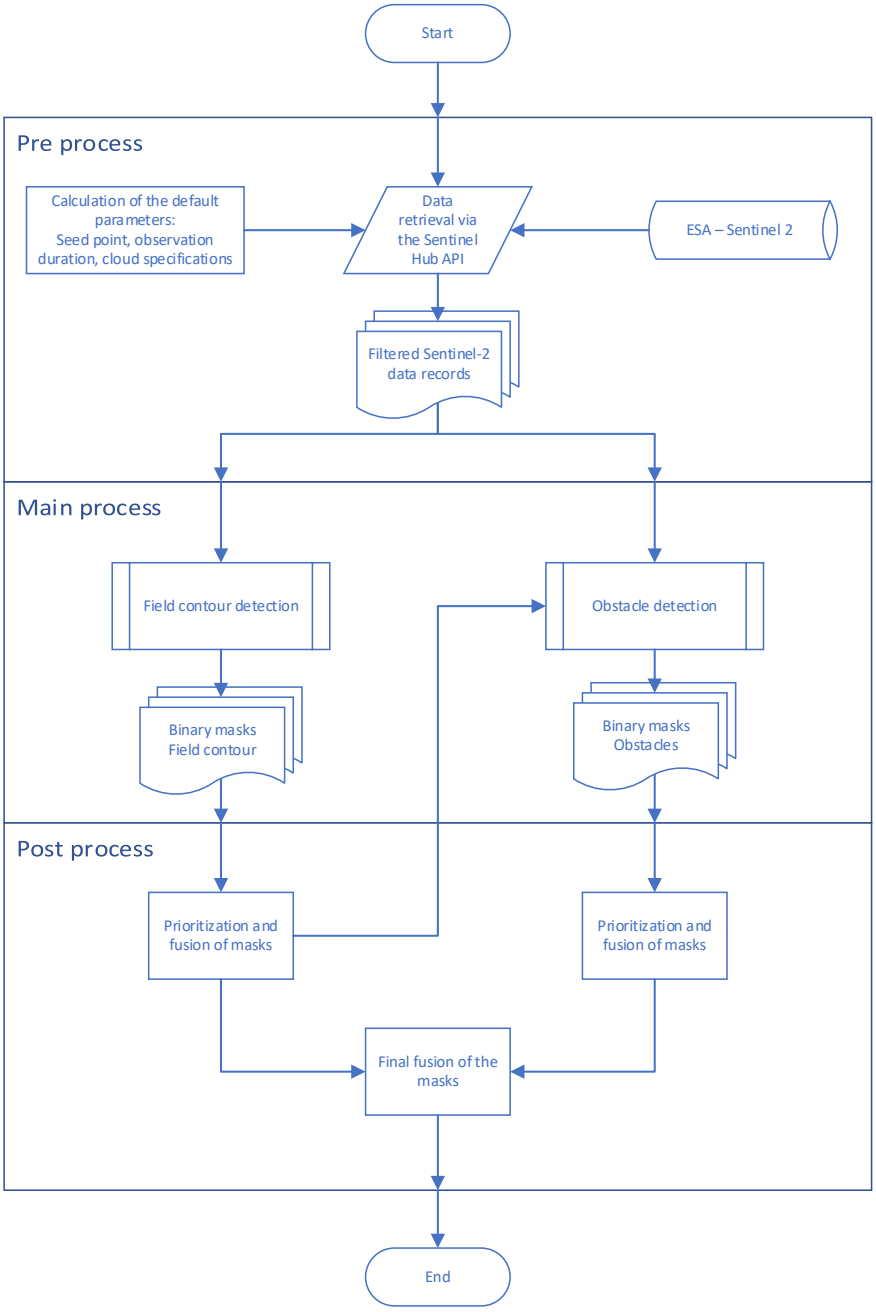

Figure 1: Flow of the overall algorithm

Pre-process

As the field contour and obstacle detection should be fully automated, it is also necessary to be able to retrieve the underlying satellite data automatically. This should also be done depending on the current GNSS position of the combine harvester to minimize the data to be requested. The Application Programming Interface (API) of the Sentinel-Hub engine from Sinergise, for example, enables the automated retrieval of data (Sinergise Ltd. 2019). To optimize the data size to be queried, a square with a side length of 3500 m is placed around the current GNSS position. This square is used as a boundary for the data to be queried and its size ensures that the field to be processed is completely enclosed. This size offers a compromise between data processing speed and coverage size, as the largest fields in the largest farm size class are assumed to be <13 ha (Jahns et al. 1983). However, as soon as the current position of the combine harvester approaches the 10% wide edge of the requested satellite data, it is requested and processed again.

A multi-temporal approach is used to minimize the influence of clouds, other environmental events and short-term local changes such as construction work. For this purpose, the most cloudless data with a maximum cloud cover of 10% from the vegetation period April to September of the last two years, including the current year, are used. The main advantage of this is that many cloud-free days are available and the decisive growth phases of the plants are covered (Deutscher Wetterdienst 2023, Karlsson et al. 2023). This means that many different plants can be reliably detected regardless of their growth behavior and the associated reflectivity for different wavelengths of light. According to initial tests with the indices under consideration, the fall and winter months do not provide promising results and are not considered further here.

Main process

There are different methods for carrying out image segmentation. Four different types of segmentation are analyzed and evaluated below as examples. The simplest method is pixel-oriented segmentation. Here, the pixel value, usually the gray value of a pixel, is compared with a predefined limit value. If the pixel value is within the value range under consideration, it is assigned to the object being searched for. This method works very efficiently when homogeneous objects are to be detected in front of a homogeneous background (Jähne 2012). Since fields and field boundaries in remote sensing data can be inhomogeneous with regard to the pixel gray value and the field is therefore poorly differentiated from the background, this approach is not expedient for detecting field contours and is only pursued further for obstacle detection.

If the shape of the object being searched for is known, model-based segmentation can be used. With the knowledge of the object shape, even partially hidden objects can be found in the image. For example, the Hough transformation can detect straight edges, even if they are interrupted. However, as agricultural fields can vary greatly in shape in reality, no generally valid shape can be specified (Jähne 2012). Meyer et. al. (2020) chose this approach, but did not achieve satisfactory results. Model-based segmentation is therefore not considered further.

Another option is edge-based segmentation. This type of segmentation uses the gray value jump at an edge to detect it. This can be determined by the first and second order derivatives. A prominent example is the Canny algorithm (Canny 1986). However, the image must first be noise-reduced using a filter, as edge-based segmentation methods are prone to noise. Subsequently, a contour tracking algorithm is necessary to obtain closed objects. In addition, further segmentation, e.g. a watershed

transformation (Vincent and Soille 1991), is necessary to reduce the detected fields to the field to be searched for (Jähne 2012, Solomon and Breckon 2011). Due to the greater complexity caused by several consecutive methods, edge-based segmentation is not considered further in this procedure.

The last type of segmentation to be considered is the region-based method. Here, pixels are compared with the neighboring pixels based on certain criteria, such as the grey value, and combined. A frequently used method is seed-based region growing, which requires one or more seed points as a reference. The functionality of this method is illustrated step by step in Figure 2. Figure 2a shows the raw image. From Figure 2b to Figure 2g, neighboring pixels of the seed point are compared and combined step by step using the seed-based region growing method.

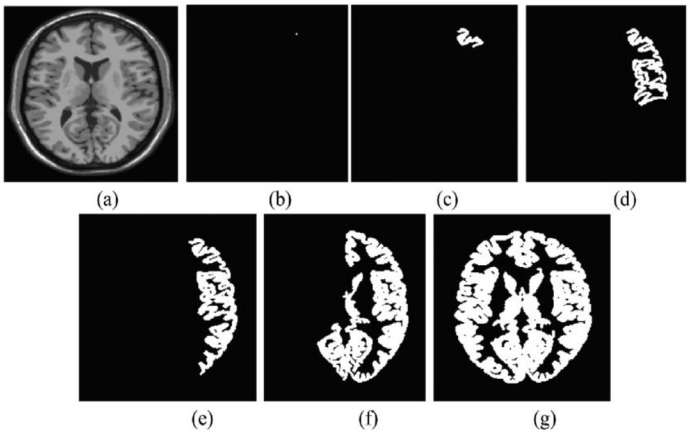

Figure 2: Region Growing (Imdad et al. 2019)

Since the seed point can be specified by the GNSS position of the combine harvester and the algorithm always outputs contiguous regions, this method is used as the basis below. In order to further optimize the results from the segmentation methods, the basic process of morphological operators is used. These primarily include erosion and dilation, which are able to change the size of the objects recognized in the image. Erosion causes a reduction in the size of existing objects, and in the process, objects may also be split. The dilation operator ensures object growth. The basic functionality is shown in Figure 3 and Figure 4.

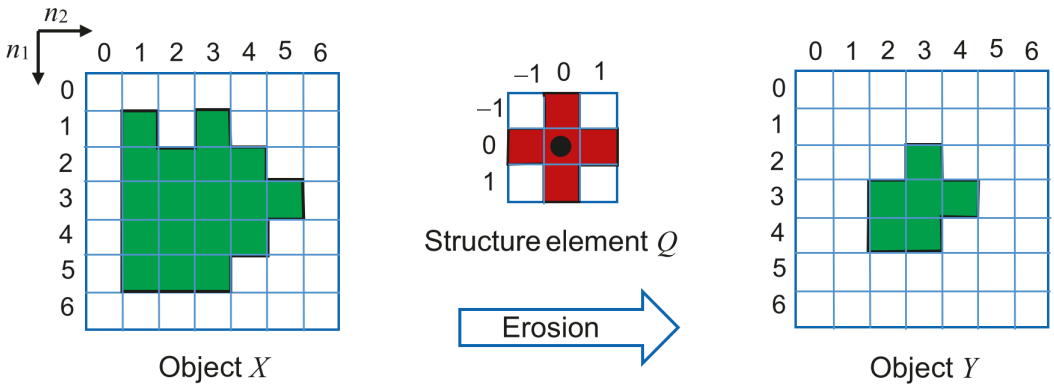

Figure 3: Erosion operation (Werner 2021)

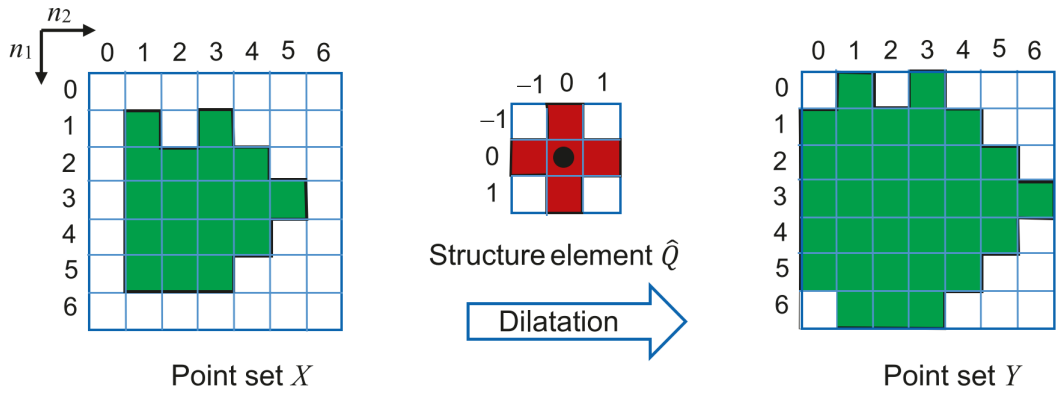

Figure 4: Dilation operation (Werner 2021)

The first step of the field contour detection algorithm is seed-based region growing, which is shown in Figure 2. Aftesr each process step, the selected pixels are stored in a mask. This method is performed at the beginning to roughly segment the area under consideration. The input parameters of this segmentation method are the seed point and the limit value of the pixel gray value. The seed point is the current GNSS position of the combine harvester. In order to make the region growing method more robust with regard to the light spectra used in the source data and the different growth phases of the plants, the limit value of the pixel gray value is dynamically adjusted or determined. This means that the value indicating the gray value at which pixels are added to the same area depends on the characteristics of the source image. This is achieved by multiplying the standard deviation of the pixel gray values of the source image by an input parameter to calculate the gray threshold value. The actual pixel gray value is already taken into account via the seed point in region growing.

Once the region growing has been completed, an erosion operation follows. This procedure makes it possible to counteract leaking segmentation in the previous step. This erosion allows regions that are only connected by thin bridges to be reliably separated. The next step is to check whether the original seed point is still located in the new area created by the erosion. If this is not the case, the source image is discarded, as the available data, in combination with the selected input parameters and the seed point, do not allow contour detection. However, if the erosion operation is successful and the seed point is still located in the newly created area, a second region growing is performed. The second region growing is only used to isolate the searched field and is applied to the resulting binary mask, thereby discarding the areas separated by the erosion operation.

In order to obtain the final recognized area, the erosion process must be reversed. A dilation operation is performed for this purpose. The parameters are optimized for the previous erosion process. Figure 5 shows this process. This area is now saved as a mask for each image and further processed into an edge mask using the Sobel operator (Sobel and Feldman 2015). This edge detection algorithm is applied to the binary mask from the previous process steps to obtain only the circumferential edges of the mask.

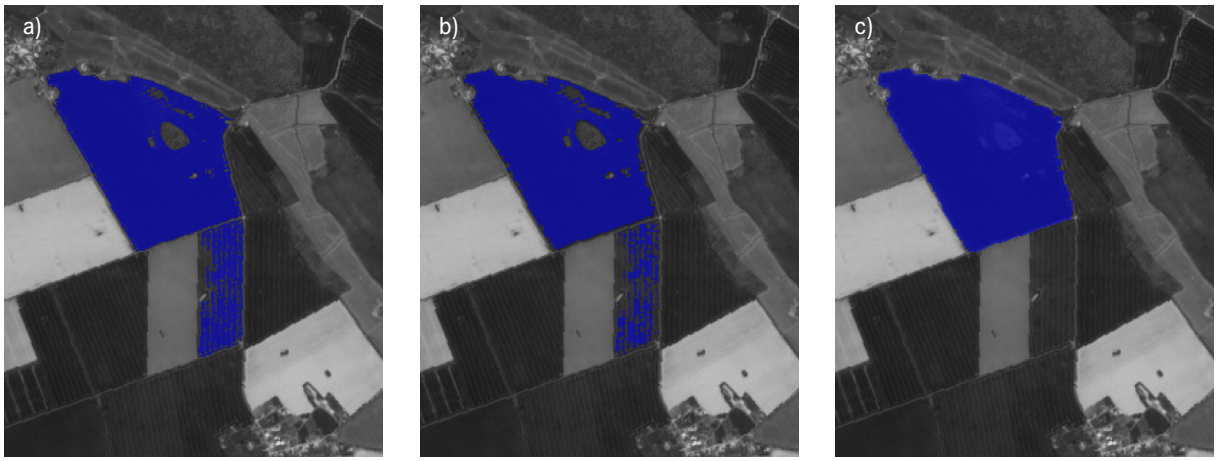

Figure 5: a) First Region Growing, b) Erosion process, c) Second Region Growing and dilation process

These process steps are repeated for each acquired image from the pre-process. The edge masks obtained in this way are prioritized or weighted based on the vegetation phases and cloud cover and merged into one mask. For this purpose, a mean value is calculated from the binary masks across all masks and compared with a threshold value. This mask is then made available to the obstacle detection algorithm. The obstacle detection algorithm differs from the contour detection in the subdivided methods. Due to the preceding contour detection, these methods can be reduced to the already detected field. This optimizes the computing time, the binarization threshold is better adapted to the relevant area and the number of possible false detections is minimized.

Initially, the respective source image is processed using a pixel-based low-pass Wiener filter. This reduces the noise components in the source image and facilitates the detection of obstacles and points of interest (POIs) (Lim 1990). The area under consideration is then binarized. This selects regions that stand out from the homogeneous crop. The Otsu method is used to determine the ideal binarization limits (Otsu 1979). This method can be used to optimize binarization and thus obstacle detection, as multiple limit values can also be determined. In the proposed method, two Otsu thresholds are calculated, and their difference is used as a criterion for further selection.

After this process step, any open structures, for example in the form of a crescent, are closed to ensure a round POI. This is made possible by dilatation and subsequent erosion. This combination of operations significantly improves the shape of the POIs, as gaps within the POIs are closed and the outer structure is rounded off.

Post-process

The post-process of the algorithm mainly involves the selection and subsequent fusion of suitable masks. The selection is based on various selection criteria.

1. Seed point position:
   If the seed point is no longer within the detected field after the field contour detection process has been completed, the affected mask is discarded.
2. Outliers:
   To increase robustness against outliers, both the masks with the smallest detection area and those with the largest detection area are discarded, as these are often instances of island detections or leakage. Additionally, all masks whose area (A_{px}) deviates by more than an empirically determined threshold from the mean area of all masks($\overline{A_{px}}$) are excluded ($A_{px} < 0.3 \cdot \overline{A_{px}}$ or $2.5 \cdot \overline{A_{px}} < A_{px}$).
3. Otsu Difference:
   The final selection criterion is the Otsu Difference. If the difference between the two calculated Otsu thresholds is not significantly distinct ($\Delta Otsu_{thresh} < 0.1$) the mask is discarded. Similar Otsu thresholds occur only in cases where the source data are visually very similar. Such data are unsuitable for obstacle detection.

After the masks have been refined through the selection process, they are merged into a single mask. The masks from the current year are given double weighting. This step is necessary because field geometry can change due to alterations in crop management by the farmer. By applying different weightings, outdated data and subsequent misdetections can be avoided.

In the next step, the calculated pixel-precise mean value of all masks, represented as a resulting grayscale value, is compared to a predefined threshold, referred to as the “pixel threshold”. If the grayscale value exceeds this threshold, the corresponding pixel is set in the fused final binary mask. This method is applied to both field contour masks and POI masks.

Results and discussion

A total of 10 different fields in northern Germany were analyzed. These fields vary in size, shape, cultivated crop, and were randomly selected. To eliminate the need for actual harvesting machine operations, the seed points were freely chosen. Manually and pixel-accurately mapped obstacles and contour boundaries served as reference data. These reference data were generated using Sentinel-2 imagery. The analyzed fields are listed in Figure 6, where the reference field contours are shown in red, and the filled POIs are depicted in blue.

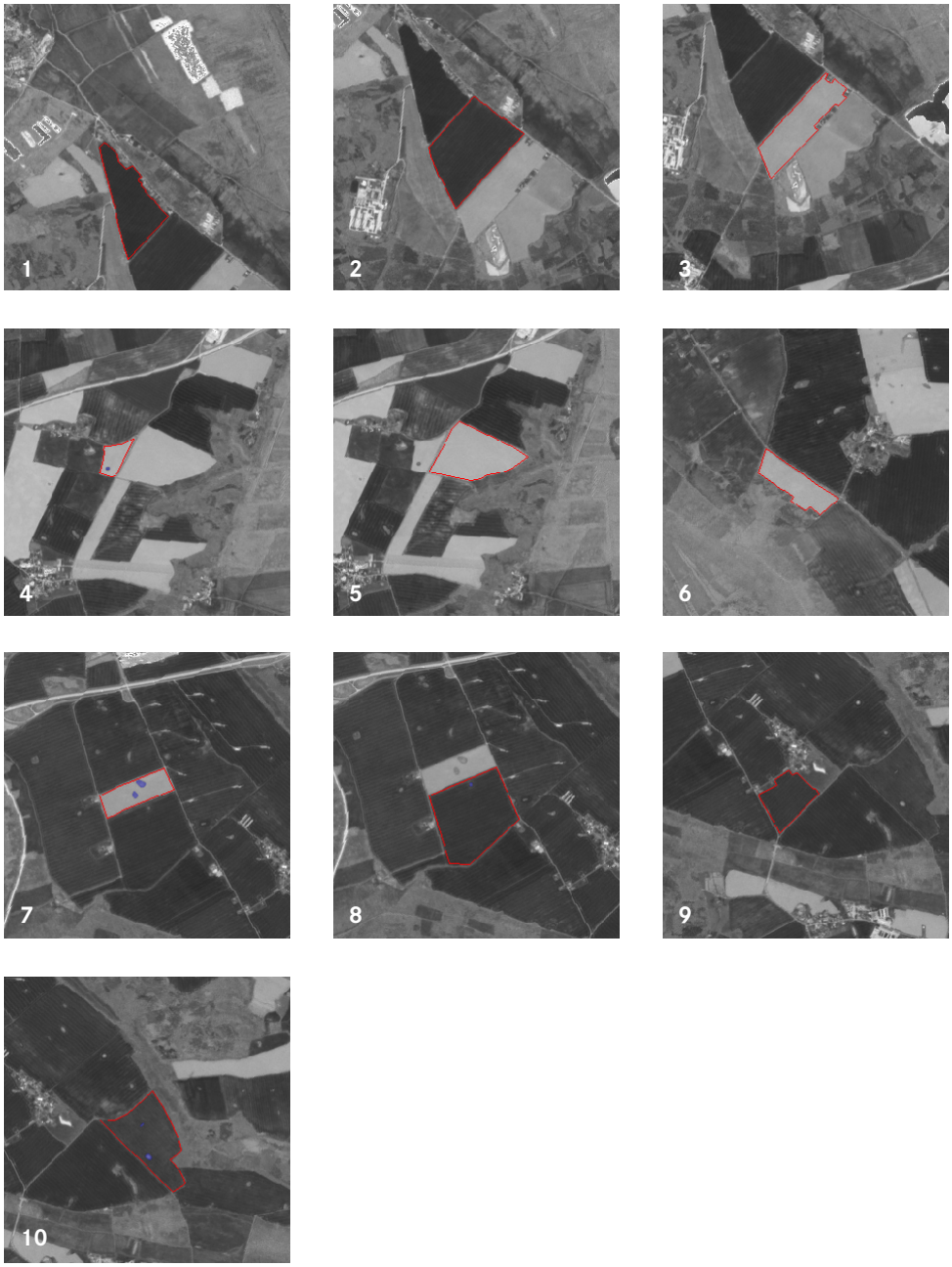

Figure 6: Analyzed fields with reference boundaries (red) and POIs (blue) using the NDWI band combination (Modified Copernicus Sentinel data 2022/Sentinel Hub)

Parameter combinations

Five different parameters, including the frequency bands, the standard deviation of the region-growing method (σ_{RG}), the strength of erosion and dilation, as well as the pixel threshold for temporal mask fusion (PT_t), were analyzed in 2,475 different combinations per field. Figure 7 provides an example of an analyzed field. To evaluate the detection quality, the Jaccard Index (JI) is used, which considers true positive (TP), false positive (FP), and false negative (FN) pixels. The JI provides a simple yet effective metric for assessing the similarity between two sets of objects and is commonly applied in image segmentation tasks (Wang et al. 2022). It accounts for both the overlap and the

differences between the detected objects. An alternative metric, for example, would be the F_1-Score, which weights *TP* differently.

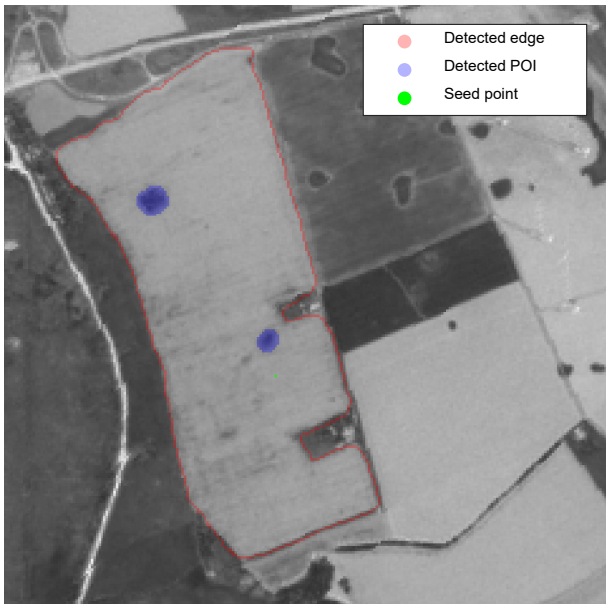

Figure 7: Detected field (Modified Copernicus Sentinel data 2022/Sentinel Hub)

Both metrics, however, measure the same aspects, which is why the *JI* is used according equation 3 (Taha and Hanbury 2015):

$$JI = \frac{TP}{TP+FP+FN} \quad \text{(Eq. 3)}$$

Firstly, the evaluation showed that the NDWI band combination delivers the best results, which is why all subsequent results are based on NDWI image data. Secondly, the erosion and dilation strength hardly changes in high-quality detections and remains at *2 px* and *4 px* ($10\,\frac{m}{px}$). Figure 8 shows the variation of results of different parameter combinations. Shown are the best and worst median as well as results that are evenly distributed between these two values to give a comprehensive overview of the full range of results. If no detection could be performed, the parameter combination was ignored. To minimize the relevance of the seed point choice, five seed points were selected for the evaluation. Care was also taken to ensure that these were not located at the immediate edge of the field, as the detection rate is significantly reduced there due to the inhomogeneous pixel environment. The free choice of seed points made it possible to dispense with an actual harvesting run. The *JI* of the respective seed points was subsequently averaged for each field. Across all ten fields, the median of the highest *JI* is 0.913. This value means that of the detected field pixels match the actual field pixels of the satellite images. This value is achieved with a parameter combination of σ_{RG} = 0.24 and PT_t = 0.4.

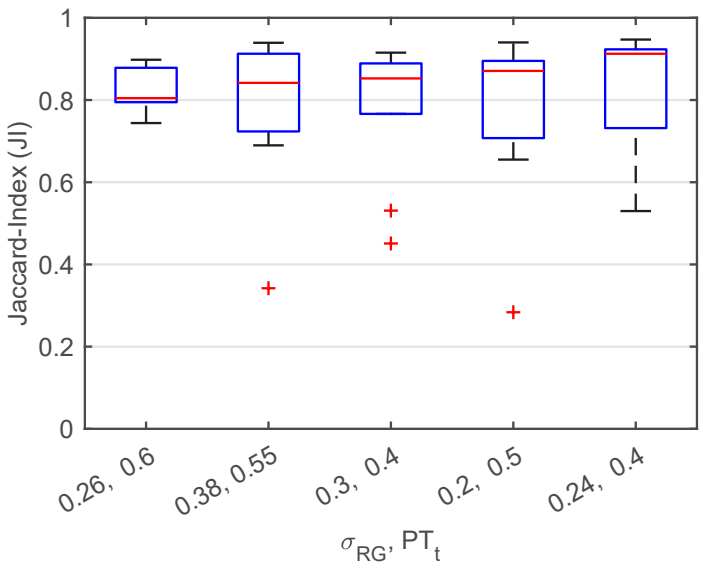

Figure 8: Comparison of different parameter combinations

In order to be able to recognize differences in the recognition quality between the individual observed fields, quality metrics frequently used in literature are shown for each field in Table 2. In addition to the *TP*, *FN*, *FP* these also include the true-negative (*TN*) pixels, the *TP* rate (*TPR* or the recall, the positive predictive value (*PPV*) or the precision and the *JI*. The table contains the results of the best parameter combination described in the previous paragraph. It is easy to see that the recognition quality depends heavily on the field under consideration. In the case of field 10 and field 7, the large number of *FP* pixels that there was a major leakage. This is also reflected in the poor *JI* of 0.53 and 0.66 respectively. Field 2, however, was clearly under-detected, which is shown by the large number of *FN* pixels. This can have a critical effect on POI detection, as these may lie outside the detected field or may also be under-detected.

Table 2: Quality metrics averaged over five seed points

Field No.	TP in px	FN in px	FP in px	TN in px	TPR / Recall in %	PPV / Precision in %	JI
1	3794.25	15.75	312.00	2245878.00	99.59	92.43	0.92
2	4420.50	1565.50	36.00	2243978.00	73.85	99.19	0.73
3	3072.75	654.25	223.50	2246049.50	82.45	93.23	0.78
4	774.67	13.34	67.33	2249144.67	98.31	92.00	0.91
5	3719.00	36.00	171.50	2246073.50	99.04	95.59	0.95
6	2209.00	134.00	59.67	2247597.33	94.28	97.38	0.92
7	1790.00	146.00	1227.50	2246836.50	92.46	70.82	0.66
8	6046.20	13.80	425.00	2243515.00	99.77	93.53	0.93
9	2170.80	29.20	151.80	2247648.20	98.67	93.50	0.92
10	4210.60	34.40	4443.80	2241311.20	99.19	52.87	0.53

Seed points

The following evaluations are based on results that were generated from each individual pixel of the source image as a selected seed point. Through this comprehensive calculation, between 788 and 6060 seed points were considered per field, corresponding to the number of pixels in the ground area of the analyzed fields. The *JI* of all seed points were then averaged for each field.

Compared to the parameter variation, the largest variance of the *JI* is achieved by the quality of the seed point selection. In order to solve this variance problem, not only is the current GNSS position selected as the seed point (SP), but six seed points on two circular paths of different radii (R1, R2) are added. The seed points are each offset by 120° to ensure the best possible coverage. Figure 9 shows this arrangement. This method can significantly increase the detection quality and thus the *JI*. This improvement is primarily due to the reduced impact of poorly placed seed points, as they can be corrected by seed points located further outward.

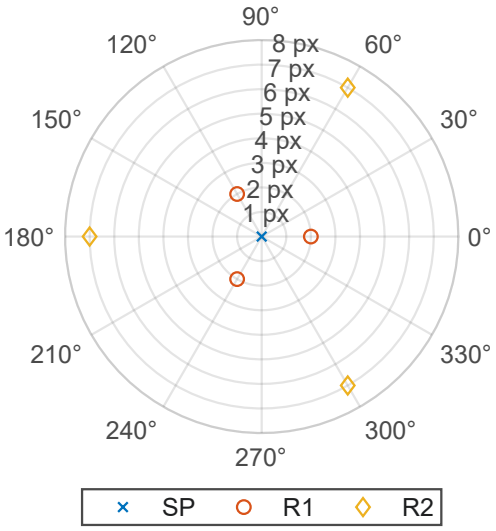

Figure 9: Seed point arrangement with multiple seed points

A comparison between a single seed point and the method with distributed seed points is shown in Figure 10. At *JI* = 0.837, the median is significantly higher than the method with a single seed point. Taking several seed points into account results in additional optimization options. Firstly, the radii of the seed point circular paths (R1, R2) can be varied, and secondly, the circular paths can be weighted differently in the mask fusion.

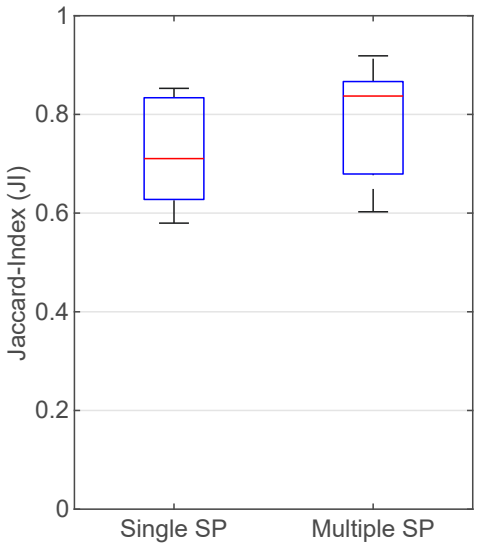

Figure 10: Comparison seed point method per field

Figure 11 shows the influence of different circular path radii r_{R1} and r_{R2}. The median of the *JI* of all fields was calculated for this figure. Since $r_{R1} > r_{R2}$ must apply, there are correspondingly fewer possible combinations. The best results can be visibly achieved with low r_{R1} values. An optimum *JI* can be achieved with r_{R1} = 2 px; r_{R2} = 7 px.

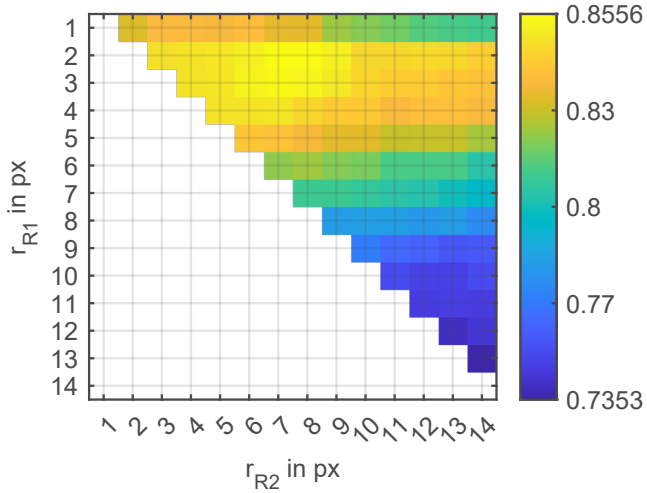

Figure 11: Influence of the orbit radii on the *JI*

A variation in the weightings of individual seed points shows no significant effect. These results are presented in Figure 12. Both the central seed point (SP) and the two surrounding circular paths (R1, R2), each with three additional seed points, were varied. The figure illustrates that even substantial modifications in the weightings have no notable impact on detection quality and, consequently, the *JI*. Therefore, a specific weighting is not a viable approach for optimization.

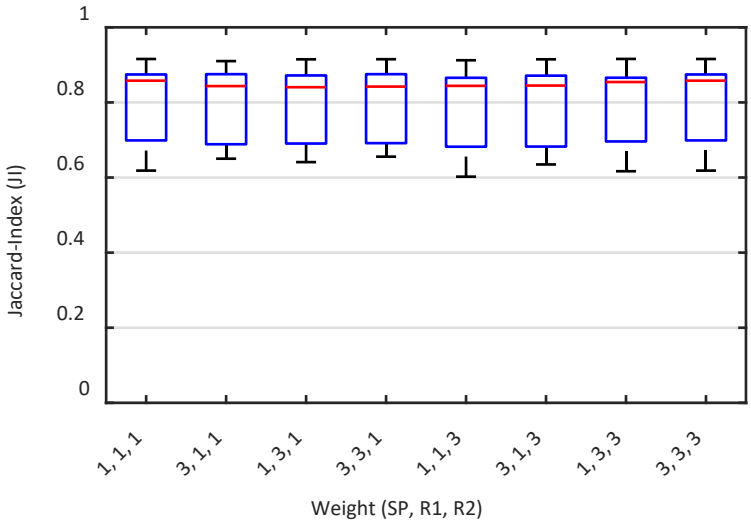

Figure 12: Comparison of the weighting of the circular paths

To conclude the discussion of the results, they are now placed in the context of previously conducted research. Wang et al. introduced a method that determines field boundaries using U-Net-based "Fully Convolutional Network (FCN)" models and achieved a *JI* of 0.801 (Wang et al. 2022). Watkins and van Niekerk (2019) combined edge detection algorithms with image segmentation methods to determine field boundaries, achieving an Overall Accuracy (OA) of 0.929. In contrast to these approaches, the method presented in this article relies on a machine-bound system. This enables the application of a seed-point-based algorithm, such as the proposed multi-temporal Seed-based Region Growing. This eliminates the need for the labor-intensive creation of training data and subsequent model training. With appropriate seed point selection and optimized process parameters, the achieved result (*JI* = 0.913) compares well with the outcomes of other methods reported in the literature.

Conclusions

The results demonstrate that, when the fundamental criteria are met and process parameters are appropriately chosen, the proposed method can effectively detect field contours and obstacles in fields with varying geometries, sizes, and crops. However, Table 2 also highlights significant differences in detection quality across the fields. Fields 10 and 7, for instance, show only minor differences from neighboring fields at their edges, which promotes undesirable leakage. Field 2, on the other hand, is under-detected, illustrating the variability in field characteristics. Apart from the quality of remote sensing data, the selection of seed points offers the greatest potential for optimization. This is evident from the observation that detection cannot proceed without a minimum quality threshold for these two criteria. Improvements are already achieved by adding additional seed points along circular paths around the current position (Figure 10). However, an appropriate selection of process parameters can also significantly influence detection quality (Figure 8).

The presented method enables the estimation of the time until critical situations, such as turning maneuvers or obstacle encounters, without requiring machine-mounted sensors. In exceptional cases, such as Fields 10 and 7, detection difficulties arose, underscoring that the method does not replace safety-critical pre-field detection but instead provides supplementary knowledge about the entire field. By integrating the current GNSS position and machine speed, the time available to the operator

before a critical situation arises can be determined. This allows for tailored task recommendations that enhance the operator's well-being and performance without compromising safety. The proposed method primarily applies to combine harvesters, as their workflows are less diverse. Future research could explore the method's applicability to other types of agricultural machinery.

To further enhance the stability and quality of detection, the following steps can be implemented in future studies.

- Leveraging commercial remote sensing data enables significantly higher resolution, allowing for finer and more precise detection of obstacles and field contours.
- Knowledge about the specific crop type in the field may improve detection, as process parameters can be tailored to the crop rather than relying on generic parameters. This could reduce variability between under-detection and over-detection in challenging fields.
- To enable more reliable detections, the system must be continuously updated as the harvesting progresses. This would allow for the inclusion of additional seed points, improving and correcting initial poor detections.
- The method could benefit from sensors carried by drones, enabling more precise investigation and classification of POIs. This would allow for targeted responses to individual obstacles. However, thanks to satellite data, there is no need for the labor-intensive task of flying drones over the entire field.

References

Airbus Defence and Space (2019): Spot – The Ideal Solution for Country-Wide, Demanding Applications. https://www.intelligence-airbusds.com/automne/api/docs/v1.0/document/download/ZG9jdXRoZXF1ZS1kb2N1bWVudC01NTMyMw==/ZG9jdXRoZXF1ZS1maWxlLTU1Mzly/spot-brochure-2019.pdf, accessed on 16 Jan 2024

Bhandari, A.K., Kumar, A., Singh, G.K. (2012): Feature Extraction using Normalized Difference Vegetation Index (NDVI): A Case Study of Jabalpur City. Procedia Technol., 2nd International Conference on Communication, Computing & Security [ICCCS- 2012] 6, pp. 612–621, https://doi.org/10.1016/j.protcy.2012.10.074

Caes, L. (2022): John Deere Reveals Fully Autonomous Tractor at CES 2022. Press release, John Deere GmbH & Co. KG. https://www.deere.com/en/our-company/digital-security/autonomous-tractor-reveal/, accessed 22 Jan 2025

Canny, J. (1986): A Computational Approach to Edge Detection. IEEE Trans. Pattern Anal. Mach. Intell. PAMI-8, pp. 679–698, https://doi.org/10.1109/TPAMI.1986.4767851

CLAAS Gruppe (2023): Innovation Lab: CLAAS zeigt auf Agritechnica 2023 nachhaltige und autonome Technik für die Landwirtschaft von Morgen und Übermorgen. Press release, CLAAS KGaA mbH, https://www.claas.com/de-de/presse/pressemitteilungen/2023-11-12-de-de-innovation-lab, accessed on 6 May 2024

Deutscher Wetterdienst (2023): RCC Node-CM Produktbeschreibung. Wolkenbedeckung. https://www.dwd.de/DE/leistungen/rcccm/int/descriptions/cfc/pds_cfc_de.pdf?__blob=publicationFile&v=16, accessed on 6 Dec 2024

DigitalGlobe (2014): WorldView-3 Data Sheet. https://www.satimagingcorp.com/satellite-sensors/worldview-3/, accessed on 16 Jan 2024

Fletcher, K. (2012): Sentinel-2: ESA's optical high-resolution missiom for GMES operational services, ESA SP. ESA communications, Noordwijk (NL)

Huete, A., Didan, K., Miura, T., Rodriguez, E.P., Gao, X., Ferreira, L.G. (2002): Overview of the radiometric and biophysical performance of the MODIS vegetation indices. Remote Sens. Environ. 83(1–2), pp. 195–213, https://doi.org/10.1016/S0034-4257(02)00096-2

Imdad, U., Asif, M., Ahmad, M., Sohaib, O., Hanif, M., Chaudary, M. (2019): Three Dimensional Point Cloud Compression and Decompression Using Polynomials of Degree One. Symmetry 11(2), 209, https://doi.org/10.3390/sym11020209

Jähne, B. (2012): Digitale Bildverarbeitung. Springer Berlin, Heidelberg, https://doi.org/10.1007/978-3-642-04952-1

Jahns, G., Steinkampf, H., Olfe, G., Schön, H. (1983): Einfluß landwirtschaftlicher Parameter auf Zeit- und Energiebedarf bei Schlepperarbeiten. Grundlagen der Landtechnik 33(4), S. 85–90, https://440ejournals.uni-hohenheim.de/index.php/Grundlagen/article/view/278, accessed on 21 Nov 2024

Karlsson, K.-G., Riihelä, A., Trentmann, J., Stengel, M., Solodovnik, I., Meirink, J.F., Devasthale, A., Jääskeläinen, E., Kallio-Myers, V., Eliasson, S., Benas, N., Johansson, E., Stein, D., Finkensieper, S., Håkansson, N., Akkermans, T., Clerbaux, N., Selbach, N., Marc, S., Hollmann, R. (2023): CLARA-A3: CM SAF cLoud, Albedo and surface RAdiation dataset from AVHRR data – Edition 3, https://doi.org/10.5676/EUM_SAF_CM/CLARA_AVHRR/V003

Kuechly, H., Cozacu, A., Kodl, G., Nicolai, C., Vallentin, C. (2020): Grundlagen der Fernerkundung. Deutsches GeoForschungsZentrum GFZ, https://doi.org/10.2312/SAPIENS.2020.001

Lim, J.S. (1989): Two-Dimensional Signal and Image Processing. Prentice-Hall signal processing series, Prentice Hall PTR, Englewood Cliffs, NJ

McFEETERS, S.K. (1996): The use of the Normalized Difference Water Index (NDWI) in the delineation of open water features. Int. J. Remote Sens. 17, pp. 1425–1432, https://doi.org/10.1080/01431169608948714

Metzger, S., Lehr, P., Ernst, V., Geimer, M. (2022a): Entwicklung einer adaptiven Benutzerschnittstelle zur Optimierung des kognitiven Benutzerzustands. In: Leibniz-Institut für Agrartechnik und Bioökonomie e.V. (Hrsg.), Arbeit unter einem DA-CH: Der Landwirt im 4.0-Modus, S. 79–90, https://opus4.kobv.de/opus4-slbp/files/17047/akal_2022.pdf#page=79

Metzger, S., Lehr, P., Geimer, M. (2022b): Stress-adaptive User Interface for the Networked Agriculture. ATZheavy Duty Worldw. 15, pp. 48–51, https://doi.org/10.1007/s41321-021-0468-5

Meyer, L., Lemarchand, F., Sidiropoulos, P. (2020): A Deep Learning Architecture for Batch-Mode Fully Automated Field Boundary Detection. Int. Arch. Photogramm. Remote Sens. Spat. Inf. Sci. XLIII-B3–2020, pp. 1009–1016, https://doi.org/10.5194/isprs-archives-XLIII-B3-2020-1009-2020

Otsu, N. (1979): A Threshold Selection Method from Gray-Level Histograms. IEEE Trans. Syst. Man Cybern. 9(1), pp. 62–66, https://doi.org/10.1109/TSMC.1979.4310076

Pascher, P., Hemmerling, U., Naß, S., Stork, S. (2020): Situationsbericht 2020/21: Trends und Fakten zur Landwirtschaft. Deutscher Bauernverband e.V., Berlin

Planet Labs (2016): RapidEye Satellite Imagery Product Specifications. https://www.satimagingcorp.com/satellite-sensors/other-satellite-sensors/rapideye/, accessed on 16 Jan 2024

Sinergise Ltd. (2019): Sentinel Hub Brochure. https://www.sentinel-hub.com/docs/Sentinel_HUB_Brochure_2019_NEW.pdf, accessed on 16 Jan 2024

Sobel, I., Feldman, G. (2015): An Isotropic 3 × 3 Image Gradient Operator. ResearchGate, https://doi.org/10.13140/RG.2.1.1912.4965

Solomon, C., Breckon, T. (2011): Fundamentals of digital image processing: a practical approach with examples in Matlab. Wiley, Hoboken, NJ

Taha, A.A., Hanbury, A. (2015): Metrics for evaluating 3D medical image segmentation: analysis, selection, and tool. BMC Med. Imaging 15(29), https://doi.org/10.1186/s12880-015-0068-x

U.S. Geological Survey (2019): Landsat 8 (L8) Data Users Handbook. https://www.usgs.gov/landsat-missions/landsat-8, accessed on 16 Jan 2024

Vincent, L., Soille, P. (1991): Watersheds in digital spaces: an efficient algorithm based on immersion simulations. IEEE Trans. Pattern Anal. Mach. Intell. 13(6), pp. 583–598, https://doi.org/10.1109/34.87344

Waard, D. (1996): The measurement of drivers' mental workload. Traffic Research Centre Univ. of Groningen, Groningen

Wang, M., Wang, J., Cui, Y., Liu, J., Chen, L. (2022): Agricultural Field Boundary Delineation with Satellite Image Segmentation for High-Resolution Crop Mapping: A Case Study of Rice Paddy. Agronomy 12, pp. 2342, https://doi.org/10.3390/agronomy12102342

Watkins, B., van Niekerk, A. (2019): A comparison of object-based image analysis approaches for field boundary delineation using multi-temporal Sentinel-2 imagery. Comput. Electron. Agric. 158, pp. 294–302, https://doi.org/10.1016/j.compag.2019.02.009

Werner, M. (2021): Digitale Bildverarbeitung. Wiesbaden, Springer Fachmedien Wiesbaden, https://doi.org/10.1007/978-3-658-22185-0

Authors

Steffen Metzger, M.Sc., is a research assistant and **Prof. Dr.-Ing. Marcus Geimer** is head of the Institute Mobile Machines (Mobima) of the Karlsruher Institute of Technology (KIT), Rintheimer Querallee 2, 76131 Karlsruhe, E-Mail: steffen.metzger@kit.edu

Notes and acknowledgements

This project was funded by the Federal Ministry of Education and Research (BMBF) as part of the strategy process “Agricultural Systems of the Future” under the funding code 031B0735.